Ultrasound in Med. & Biol., Vol. 28, No. 3, pp. 359–368, 2002

0301-5629/02/$–see front matter

PII: S0301-5629(01)00510-5

● *Original Contribution*

ESTIMATING THE ELASTOGRAPHIC SIGNAL-TO-NOISE RATIO USING CORRELATION COEFFICIENTS

S. SRINIVASAN, F. KALLEL and J. OPHIR

The University of Texas Medical School, Department of Radiology, Ultrasonics Laboratory, Houston, TX, USA; and University of Houston, Electrical and Computer Engineering Department, Houston, TX, USA

(*Received* 20 *August* 2001; *in final form* 4 *December* 2001)

Abstract—In conventional elastography, strain is estimated from the gradient of the displacement (time-delay) estimates. The displacement estimates involve estimating the peak location of the cross-correlation function between matching pre- and post-compression A-lines. Bias errors in estimating the peak location of the cross-correlation function, amplified by the gradient operation on the displacement estimates (needed for the computation of the strain), could result in values of elastographic signal-to-noise ratio (SNR_e) that exceed the theoretical upper bounds, thereby hindering a consistent interpretation of this parameter. These algorithmic errors have not been accounted for by the theory. We propose the use of the measured correlation coefficients in the theoretical SNR_e expressions to estimate the SNR_e, rather than computing them directly from the elastograms. This methodology results in values of SNR_e that are lower than the theoretical upper bounds, thereby avoiding the problems associated with computing SNR_e directly from the elastograms. Using simulated models of uniformly elastic phantoms, a proof of principle of such an SNR_e measure is shown. (E-mail: Jonathan.Ophir@uth.tmc.edu)

Key Words: **Ultrasound, Elastography, Correlation coefficient, SNR.**

INTRODUCTION

Ultrasonic techniques for measuring the elastic properties of compliant tissue generally rely on the estimation of strain. Elastography, a technique of estimating strain using differential displacements of the tissue elements has been well established (Ophir et al. 1991, 1996, 1997, 1999). The commonly used time-domain cross-correlation techniques estimate the time delay between the pre- and the post-compression radiofrequency (RF) A-lines. The strain is estimated as the gradient of the time-delay. Stretching the post-compression A-lines is typically done to undo the effects of the mechanical compression on the signal (Cespedes and Ophir 1993; Varghese and Ophir 1997a). This stretching improves the correlation between the pre- and post-compression A-lines and reduces the strain noise. However, a perfect match between the pre- and post-compression A-lines is not achievable. This is because the transmitted pulse gets stretched simultaneously when the stretching compensates for the tissue motion. The decorrelation of the A-lines increases with the applied strain (Varghese and Ophir 1997a) and corrupts the strain estimates for large strains (typically $> 10\%$). On the other hand, for very low strains (typically $< 0.1\%$), the strain estimates are affected by the sonographic signal-to-noise ratio (SNR_s). Hence, there is an intermediate range of strains for which good elastographic SNR (SNR_e) (defined as the ratio of the mean value (μ_s) of the estimated strain to the SD of the estimated strain (σ_s)) can be obtained. The behavior of the SNR_e as a function of the axial tissue strain (Fig. 1) is similar to a band-pass filter (in the strain domain) and has been named the Strain Filter (SF) (Varghese and Ophir 1997b). A brief introduction to the SF is given below.

Theoretical expressions for the upper bounds of SNR_E

The expression for the upper bound of the SNR_e is given by:

$$SNR_e = \frac{s}{\sigma_s} \tag{1}$$

where s is the applied strain and σ_s is the lower bound on

Address correspondence to: Jonathan Ophir, The University of Texas Medical School, Department of Radiology, Ultrasonics Laboratory, 6431 Fannin St., Houston, TX 77030 USA. E-mail: Jonathan.Ophir@uth.tmc.edu

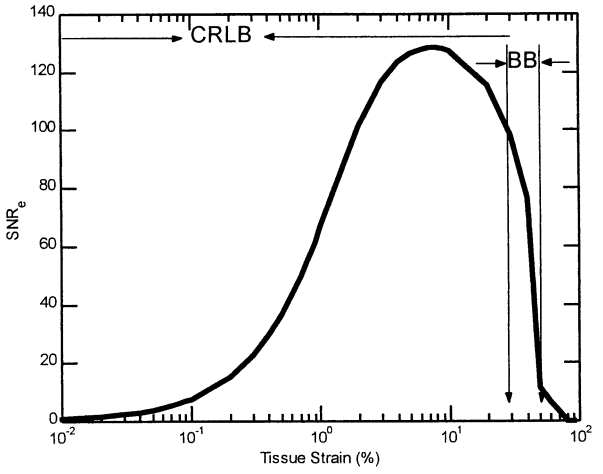

Fig. 1. The SF illustrating the distinct regions of strain estimation obtained using the expressions for σ_{ZZLB}. The SF was obtained for a 5-MHz, 50% fractional bandwidth transducer using an observation window of 3 mm and a window overlap of 1.5 mm at an SNR_s of 30 dB. The *CRLB* refers to the Cramer–Rao lower bound that is dominated by random noise. The *BB* refers to the Barankin bound that is dominated by decorrelation noise.

the SD of the measured strain given in Cespedes et al. (1995b) as:

$$\sigma_s^2 = \frac{2\sigma_t^2}{T\Delta T} \tag{2}$$

where T is the segment length, ΔT is the separation between adjacent time segments and $\sigma^2{}_t$ is the variance in the temporal time-delay estimate. The lower bound on $\sigma^2{}_t$ is derived in Weinstein and Weiss (1984a, 1984b) as the Ziv–Zakai lower bound ($\sigma^2{}_{ZZLB}$) and has been adapted to elastography by Varghese and Ophir (1997b) as:

$$\sigma^2_{ZZLB} = \begin{cases} \dfrac{(sT)^2}{6T\Delta T}, & BTSNR_c < \gamma \\ Threshold_1, & \gamma < BTSNR_c < \delta \\ 2\dfrac{\sigma^2_{BB}}{T\Delta T}, & \delta < BTSNR_c < \mu \\ Threshold_2, & \mu < BTSNR_c < \eta \\ 2\dfrac{\sigma^2_{CRLB}}{T\Delta T}, & \eta < BTSNR_c \end{cases} \tag{3}$$

Here, B is the system bandwidth, and SNR_c is the combined SNR used in obtaining σ_{ZZLB}, defined as:

$$SNR_c = \frac{SNR_\rho SNR_s}{1 + SNR_\rho + SNR_s} \tag{4}$$

where SNR_s is the sonographic SNR, and SNR_ρ is the correlation SNR (Cespedes and Ophir 1993), given by:

$$SNR_\rho = \frac{\rho}{1-\rho} \tag{5}$$

Details on the several variance values (σ_{CRLB}, σ_{BB}, $Threshold_1$, $Threshold_2$) and the bounds η, γ, δ, μ, can be found in Varghese and Ophir (1997b) as:

$$\eta = \frac{12}{\pi^2 T\Delta T}\left(\frac{f_0}{B}\right)^2\left[\phi^{-1}\left(\frac{B^2}{24f_0^2}\right)\right]^2 \tag{6}$$

$$\mu = \frac{5.52}{\pi^2 T\Delta T}\left(\frac{f_0}{B}\right)^2 \tag{7}$$

$$\delta = \zeta/T\Delta T \tag{8}$$

$$\gamma \approx 0.92/T\Delta T \tag{9}$$

where

$$\phi(y) = \frac{1}{\sqrt{2\pi}}\int_y^\infty e^{-\mu^2/2}d\mu, \tag{10}$$

and

$$(\zeta/2)\phi(\sqrt{\zeta/2}) = (12\pi/BsT)^2 \tag{11}$$

The theoretical expression for the variation of ρ with strain has been established in Varghese and Ophir (1997a) and is given by:

$$\rho = \left(\frac{\sqrt{2(1-s)}}{(1+e^{-(lk_0)^2})\sqrt{(1-s)^2+1}}\right) \times \left(e^{-\left(\frac{(lk_0)^2}{2}\frac{s^2}{((1-s)^2+1)}\right)} + e^{-\left(\frac{(lk_0)^2}{2}\frac{(2-s)^2}{((1-s)^2+1)}\right)}\right) \tag{12}$$

where s is the applied strain, k_o is the wave number (given by $k_o = 2\pi/\lambda_o$ where λ_o is the wavelength), and l is the correlation length. Combining eqns (1) through eqn (12), we obtain the functional dependence of the upper bound of SNR_e on s. Such a variation of SNR_e with s has a band-pass characteristic, as shown in Fig. 1. Two bounds, namely the Cramér–Rao lower bound (*CRLB*) and the Barankin bound (*BB*) are shown. The

CRLB corresponds to the region where there are no ambiguities in the amplitude and phase measurement and the *BB* corresponds to the region where ambiguities in phase measurement exist.

The variance in the time-delay estimation achieves the Ziv–Zakai lower bound for unbiased estimators that involve time domain correlation of analog signals. Estimating time delays between discrete signals is typically done through interpolation between samples (to avoid oversampling of the A-lines, and thereby reduce the computational cost and the acquisition time) around the cross-correlation peak location, because the peak does not necessarily fall at the exact sample locations. Typical interpolation techniques involve a three-point parabolic or cosine interpolation around the peak sample (Cespedes et al. 1995a; De Jong et al. 1990). These techniques have been shown to be biased and result in image artefacts such as image periodicities commonly known as "zebras and worms" (Ophir et al. 1999; Cespedes 1993). A detailed analysis of these bias errors has been done by Cespedes et al. (1995a), and some of the effects of these bias errors are briefly explained below.

Bias errors in time-delay estimation in elastography

In elastography, stretching the post-compression A-lines is done before time-delay estimation between the pre- and post-compression A-lines to remove the effects of mechanical compression on the signals. Hence, for a uniformly elastic phantom and in the absence of noise, zero time delays between the pre- and post-compression A-lines are expected after a perfect stretching of the post-compression A-line. However imperfect stretching of the post-compression A-line (Varghese and Ophir 1997a; Cespedes 1993) and the presence of noise in the A-lines result in small random subsample delays (δ). Previous work has shown that the bias errors for subsample delays are periodic with a period of 1 sample, nulls occurring at $\delta = 0.5$ and 0 samples and a maximum around $\delta = 0.3$ samples (Cespedes et al. 1995a).

Adjacent A-line segments tend to have similar bias errors (especially when a high overlap between adjacent segments is used) resulting in image artefacts (Ophir et al. 1999; Cespedes 1993). This results in smoother strain estimates and, hence, high SNR_e. To illustrate this, consider a case where no subsample time-delay estimate (TDE) is found (*i.e.*, the sample corresponding to the correlation peak is taken as the true TDE). For such a case, the TDE on a uniformly elastic phantom would most likely fall at the same sample location (the first sample, if there is no shift between the A-lines) for each segment. Hence, the strain estimates for all the segments would be identical to each other, resulting in an infinite SNR_e. Such a result is misleading because the presence of noise and imperfect stretching should result in finite

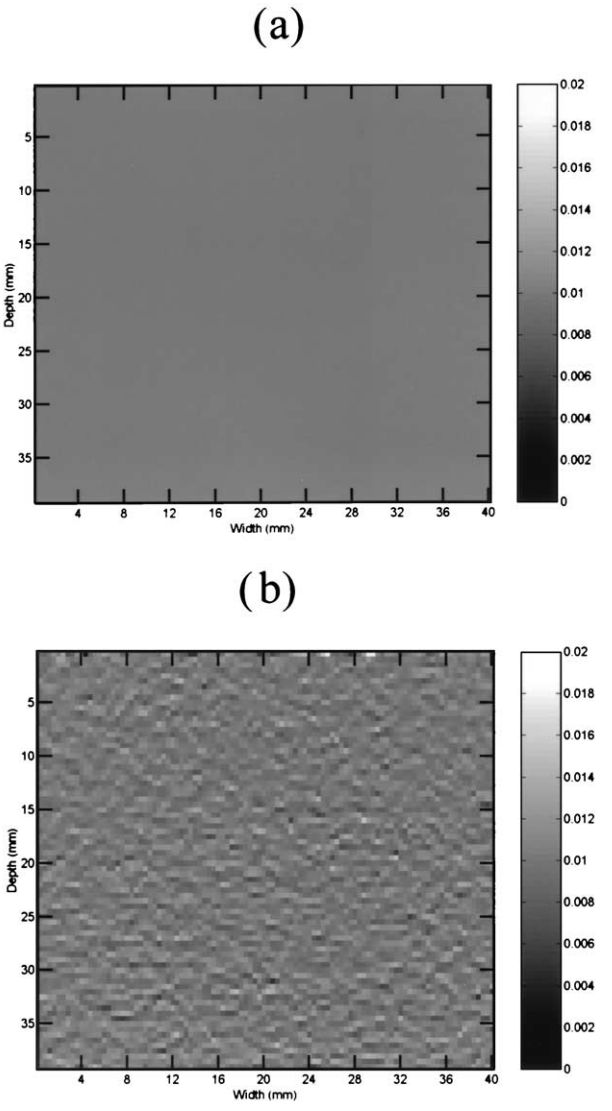

Fig. 2. Elastograms simulated using a 5-MHz, 35% fractional bandwidth transducer, and 1-mm window with a 50% overlap on a uniformly elastic phantom of 40×40 mm^2 at 1% applied strain with (a) no interpolation, and (b) parabolic interpolation.

SNR_e. Figure 2a shows such a case where the strain is estimated with no subsample interpolation (an extreme case of biased interpolation) and Fig. 2b shows the case where subsample interpolation is done. The presence of additive noise and imperfect stretching produces residual time-delay uncertainties and, hence, a nonuniform strain image that can be seen in Fig. 2b. However, the absence of such strain nonuniformities in Fig. 2a is due to the lack of interpolation (precision in the time-delay estimation) and is not indicative of the detail in the strain image. This lack of precision usually results in loss of structural detail in the elastogram that is significant, especially when there is a strain contrast (like hard or soft inclu-

sions in a uniformly elastic phantom). For example, for the case of a hard inclusion in a uniformly elastic phantom, the absence of subsample interpolation to estimate the TDE could result in the loss of contrast and, hence, problems in lesion detectability. Figure 3 illustrates such a loss of contrast in the absence of interpolation. The inclusion cannot be seen in Fig. 3a, where subsample interpolation is not performed, but it can be clearly seen in Fig. 3b, where subsample interpolation is performed. The value of the correlation coefficient improves with interpolation, as can be seen in Fig. 3c, where a map of the difference in the correlation coefficients between the cases of subsample interpolation and no subsample interpolation is shown. Such a result is expected because subsample interpolation improves the value of the correlation coefficient. Thus, as detailed later, the correlation coefficient can be used to reliably predict the SNR_e. A systematic study of the effects of biased interpolation on the loss of image contrast is beyond the scope of this work.

As illustrated above, biased interpolation could result in high SNR_e that does not represent the signal decorrelation between the pre- and post-compression RF A-lines. Moreover, visible elastographic artefacts such as "zebras and worms," which occur due to biased interpolation, affect the SNR_e estimate from the elastogram as well. Hence, an SNR_e measure that avoids such image-related problems is preferable. One such measure using ρ is detailed below.

Using the correlation coefficient to compute SNR_e

The estimated value of ρ is used in eqn (5) to compute the SNR_ρ. This computed value of SNR_ρ is used in eqn (4) to compute the SNR_c which, in turn, is used in eqn (3) to estimate the σ_{ZZLB}. Equation (2) is then used to compute the lower bound on σ_s (the lower bound is obtained when $\sigma_t = \sigma_{ZZLB}$) and eqn (1) uses σ_s to compute the SNR_e.

1-D simulations of uniformly elastic phantoms were conducted and the results are summarized below. Figure 4a shows the theoretical values of ρ as a function of strain, eqn (6) along with the computed values. It can be seen that the computed values of ρ are lesser than the theoretical values at all strains. There is an improvement in the estimated value of ρ with the use of interpolation (Fig. 4b). A statistical analysis was performed to show that the mean values of the correlation coefficients at several sampling frequencies differed from each other (p-values < 0.01) at strains less than 6%. For higher strains ($> 6\%$) no statistically significant difference was found (p-values > 0.1). Fifty independent realizations were used.

A comparison of the theoretical values of the SNR_e with the ones estimated using ρ and those computed directly from the elastogram is shown in Fig. 5. It can be seen that there is a good agreement between the SF that uses the estimated value of ρ and that predicted theoretically (the upper bound). The SF that is computed directly from the elastogram exceeds the theoretical upper bounds for reasons explained previously. The mean values of SNR_e obtained directly from the elastogram differed from those obtained using the correlation coefficients (p-values < 0.01) in some regions of the SF (strains ranging from 4% to 20% and strains $< 0.2\%$). For strains ranging between 0.2% and 4%, no statistically significant difference was found (p-values > 0.1).

The value of ρ decreases with the lack of interpolation (Fig. 4b) and results in a decrease in SNR_e. However, the improvement in SNR_e with interpolation is marginal, as can be seen in Fig. 6. This indicates the robustness of the technique with respect to the interpolation scheme and also the lower sensitivity to bias errors in TDE.

The utility of ρ as an estimator of SNR_e is tested by changing several parameters like the SNR_s, center frequency (f_o), bandwidth (B), segment size (T), and segment separation (ΔT). The results for increasing SNR_s are shown in Fig. 7a. A good match between the theory and the simulations can be seen. Figure 7b shows the improvement of the SF with the center frequency of the transducer. Because the SNR_e has a 3/2 power relationship with the center frequency (*i.e.*, $SNR_e \propto f_o^{3/2}$ (Varghese and Ophir 1997b)), the SF improves in both the SNR_e and the dynamic range (defined as the range of strains in which the SNR_e exceeds a predefined value). Similar improvements can be seen with the bandwidth (B), segment size (T), and segment separation (ΔT) in Figs. 8a, b, and c, respectively.

2-D simulations of uniformly elastic phantoms were conducted in MATLAB to further corroborate the results. Figure 9a shows the theoretical (Kallel et al. 1997) and the simulated SFs at different lateral locations for the simulations on a 40×40 mm^2 uniformly elastic phantom with a 100-element array transducer (pitch = 0.4 mm) and a Gaussian beam profile of beamwidth (half-amplitude) of 0.7 mm. The SF at the location of lateral symmetry (20 mm) has smaller values of the SNR_e and dynamic range than those corresponding to the 1-D simulations. This is attributed to the nonrigid scatterer motion (in the lateral direction) within the beamwidth. The values of ρ corresponding to the SFs in Fig. 9a are shown as a function of strain in Fig. 9b. Figure 9c shows the correlation coefficient as a function of the lateral location. The change in the values of ρ with the lateral location are similar to those obtained by Kallel et al. (1997). A statistical comparison of the SFs over 50 realizations was performed to compare SFs based on a 95% confidence interval (p-value < 0.01). The true

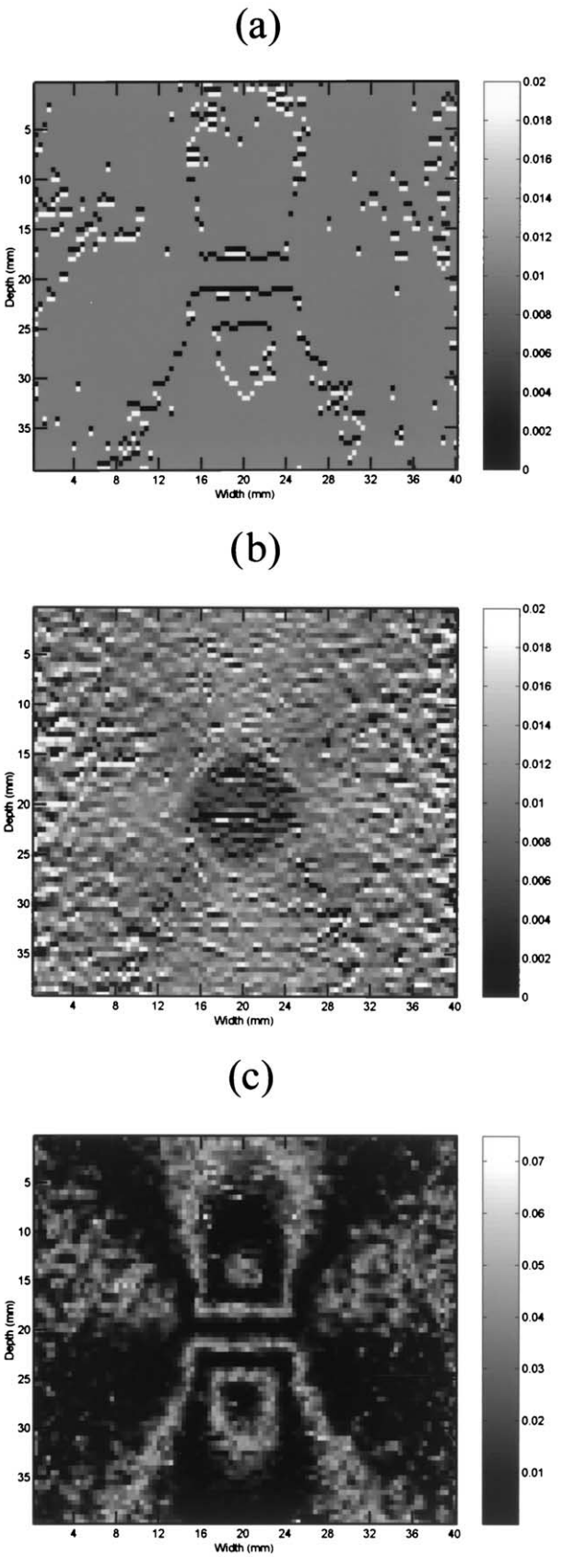

Fig. 3. Elastograms simulated using a 5-MHz, 35% fractional bandwidth transducer, and 1-mm window with a 50% overlap on a 40 × 40 mm^2 phantom, with a 5-mm radius inclusion and a modulus contrast of 3, at 1% applied strain with (a) no interpolation, and (b) parabolic interpolation. (c) The difference in the correlation maps corresponding to the elastograms obtained using parabolic interpolation and no interpolation. A sampling frequency of 48 MHz and a SNR_s of 40 dB were used.

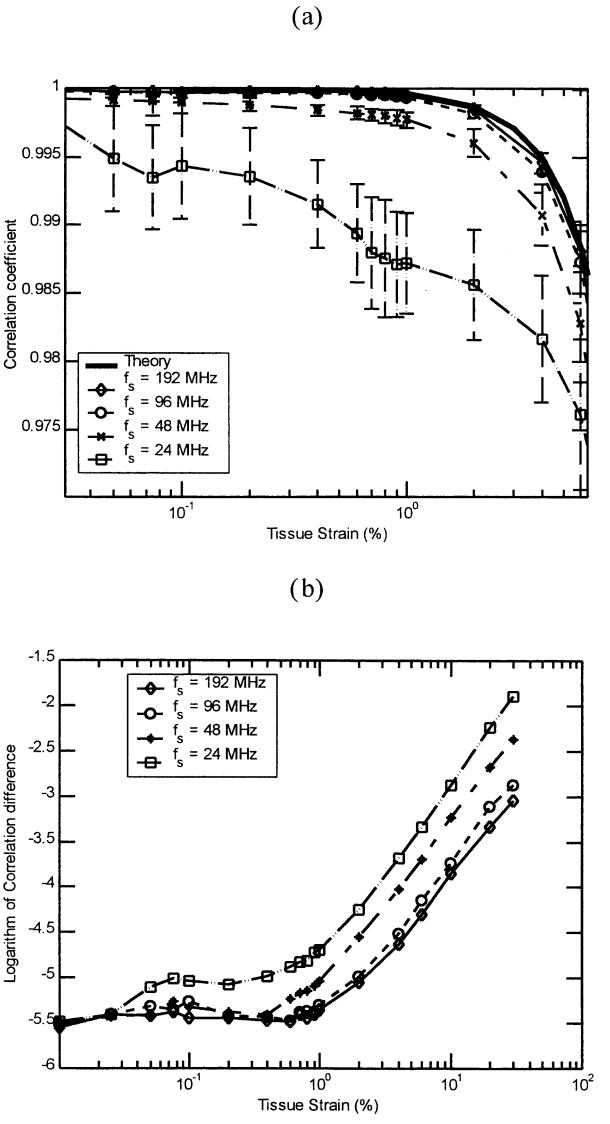

Fig. 4. (a) The theoretical and the estimated correlation coefficients for various sampling frequencies (f_s) and (b) improvement in the correlation coefficient with interpolation shown as the logarithm of the difference in the correlation coefficient with and without interpolation, for a 5-MHz, 50% fractional bandwidth Gaussian PSF, and 3-mm window with a 50% overlap on a uniformly elastic phantom at a SNR_s of 40 dB. Here, the error bars correspond to $\pm$ σ over 50 realizations.

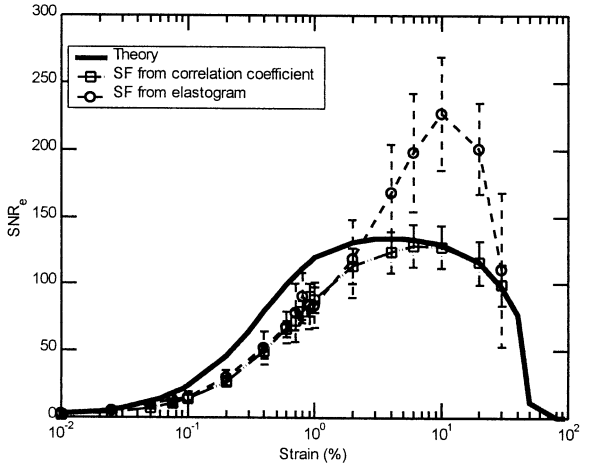

Fig. 5. Comparison of the SFs obtained using the correlation coefficient and image SNR_e with the theoretical SF for a 5-MHz, 50% bandwidth Gaussian PSF, and 3-mm window with a 50% overlap on a uniformly elastic phantom at a SNR_s of 40 dB and a sampling frequency (f_s) of 96 MHz. The error bars correspond to $\pm$ σ over 50 realizations.

means of the simulated SFs were found to be significantly different from one another for those reported in Figs. 7, 8 and 9. The above-mentioned results further validate the use of the ρ as an estimator for SNR_e.

DISCUSSION

The previous sections dealt with the pitfalls in computing the SNR_e directly from the elastogram and also

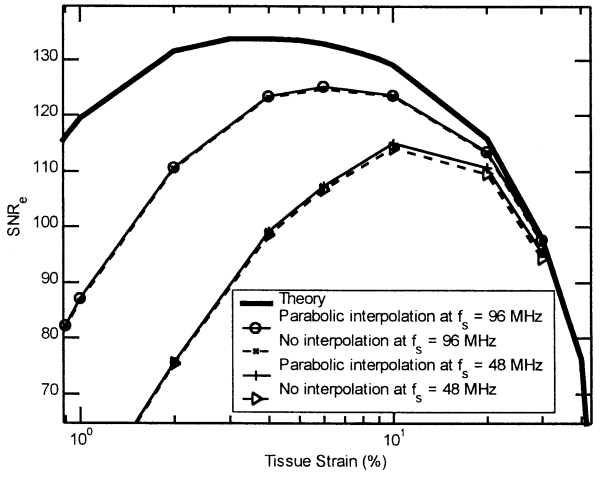

Fig. 6. Comparison of portions of the SFs obtained using the correlation coefficient for the schemes with no interpolation on the cross-correlation peak and parabolic interpolation on the cross-correlation peak. The simulations were performed on a 5-MHz, 50% bandwidth Gaussian PSF, and 3-mm window with a 50% overlap on a uniformly elastic phantom at a SNR_s of 40 dB and sampling frequencies (f_s) of 48 MHz and 96 MHz.

(a)

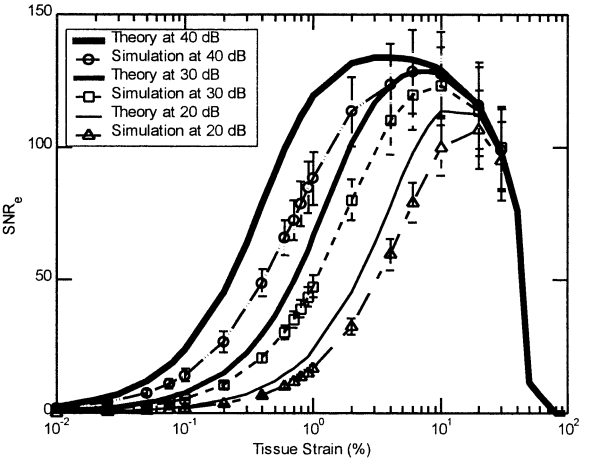

(b)

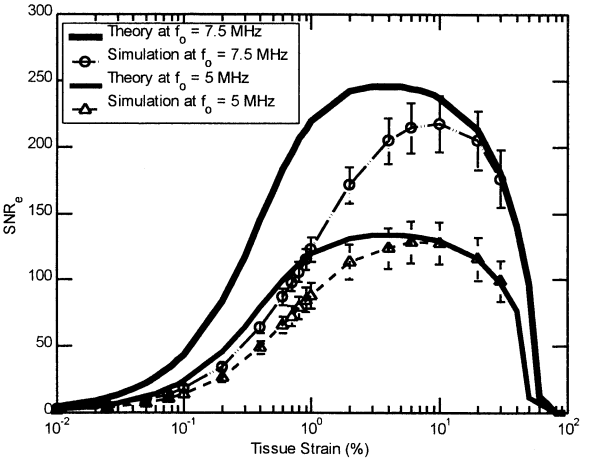

Fig. 7. SFs for (a) several values of SNR_s and (b) several center frequencies for a 5-MHz, 50% fractional bandwidth Gaussian PSF, and 3-mm window with a 50% overlap on a uniformly elastic phantom at a SNR_s of 40 dB and a sampling frequency (f_s) of 96 MHz. The error bars correspond to $\pm$ σ over 50 realizations.

with the use of ρ as a robust estimator of SNR_e indirectly from the elastogram. Yet, the value of ρ does not have a one-to-one correspondence with the visual image (estimated through a gradient of the TDE) because a small change in the correlation coefficient could result in significantly different strains, as evident from Fig. 4. However, using ρ to estimate SNR_e facilitates a direct comparison between theory, simulations and experiments, and could be used as a benchmark in comparing algorithms and apparatus.

The 2-D simulations produce SFs that have smaller SNR_e and dynamic range than the 1-D simulation. This is

(a)

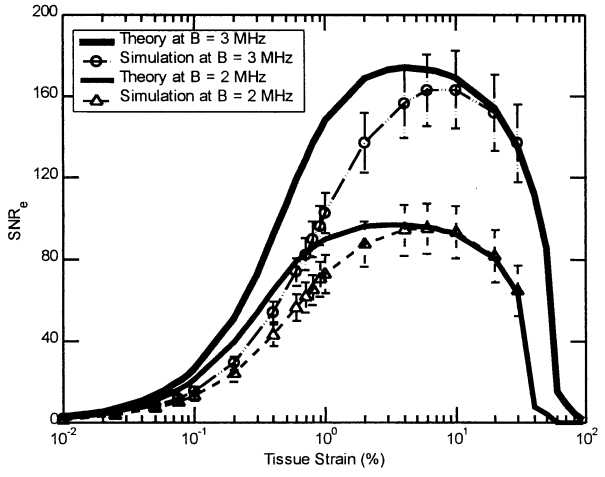

(b)

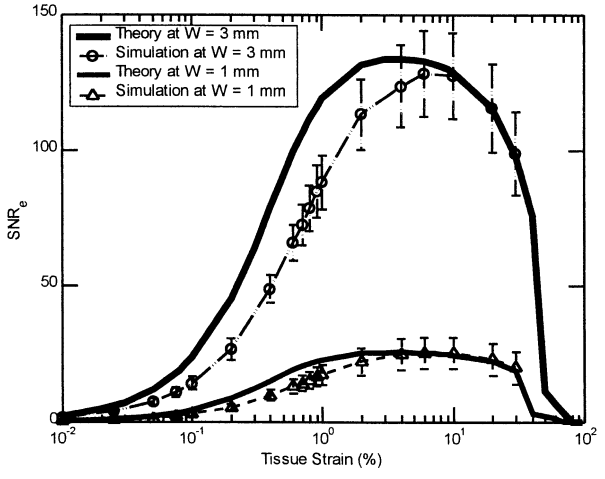

(c)

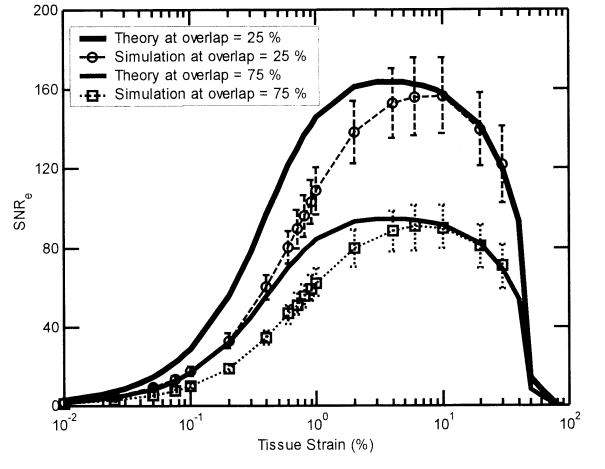

due to the lateral motion and the presence of a beam in the 2-D simulation. It is to be noted that derating the SFs to accommodate lateral motion (Kallel et al. 1997) still does not account for the nonrigid scatter motion within the beam. Therefore, the SFs at the location of lateral symmetry (*i.e.*, at 20 mm in Fig. 9a) is poorer than the 1-D simulation. An analysis of nonuniform displacement within the beamwidth needs to be done to account for such difference between the theoretical and simulation results.

The use of subsample interpolation improves the values of ρ because the subsample peak value tends to be larger than that corresponding to the sample peak. Figure 10a and b show the correlation maps corresponding to Figs. 3a and b, respectively. The improvement in the values of ρ with subsample interpolation is evident from these figures. It is of interest to note that some adaptive stretching techniques (Alam et al. 1998; Bilgen 1999) utilize the maximum value of ρ to estimate the stretch factor (and, hence, the strain) and thereby improve the SNR_e in the presence of strain contrast. These adaptive stretching techniques have shown the values of ρ (and SNR_e) to improve with adaptive stretching. The stretch factor corresponding to the maximum value ρ reflects the local strain and, thus, eqns (1) through (5) could be used to compute the local SNR_e. Hence, the improvement of ρ represents the improvement in the local SNR_e. The SNR_e maps corresponding to those in Fig. 3a and b are shown in Figs. 11a and b, respectively. Here, the analytical strain map (Kallel et al. 1996) was used to compute the SNR_e values. Low values of SNR_e in the regions corresponding to the inclusion can be seen in these figures because the strain in these regions are low and the variance is high. The difference in the SNR_e between Fig. 11b and a are shown in Fig. 11c. The positive values indicate the improvement in SNR_e, as well as the correspondence between the local values of SNR_e and ρ.

A phantom with strain contrast would be less suitable than a uniformly elastic phantom for benchmarking (in terms of the SNR_e) because strain contrast is more a test of the stretching (companding) schemes. Moreover, upper bounds for the values of the contrast-to-noise ratio (CNR_e) in the presence of strain contrast can be obtained directly from the SF (Varghese and Ophir 1998). (These upper bounds can be achieved with the use of adaptive strain estimation procedures because a uniform stretch-

Fig. 8. SFs for (a) several fractional bandwidths, (b) several window lengths, and (c) several window overlaps for a 5-MHz, 50% fractional bandwidth Gaussian PSF, on a uniformly elastic phantom at a SNR_s of 40 dB and a sampling frequency (f_s) of 96 MHz. The error bars correspond to $\pm \sigma$ over 50 realizations.

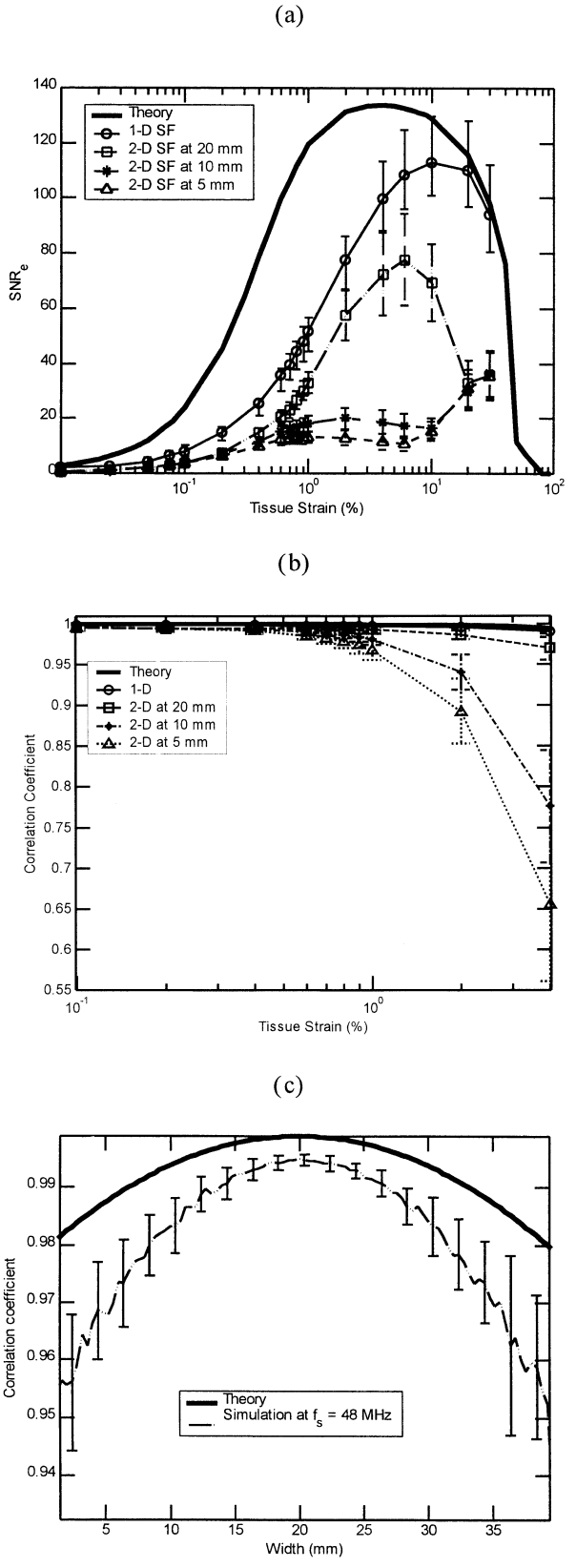

Fig. 9. (a) 2-D SFs at several lateral locations and comparison with the theoretical and 1-D SFs, (b) the correlation coefficient as a function of strain at several lateral locations, and (c) the correlation coefficients as a function of the lateral location for a strain of 1%. The simulations were performed on a 40 × 40 mm^2 uniformly elastic phantom with a 5-MHz, 50% fractional bandwidth Gaussian PSF, and 3-mm window with a 50% overlap at a SNR_s of 40 dB and a sampling frequency (f_s) of 48 MHz. The error bars correspond to ± σ over 50 realizations.

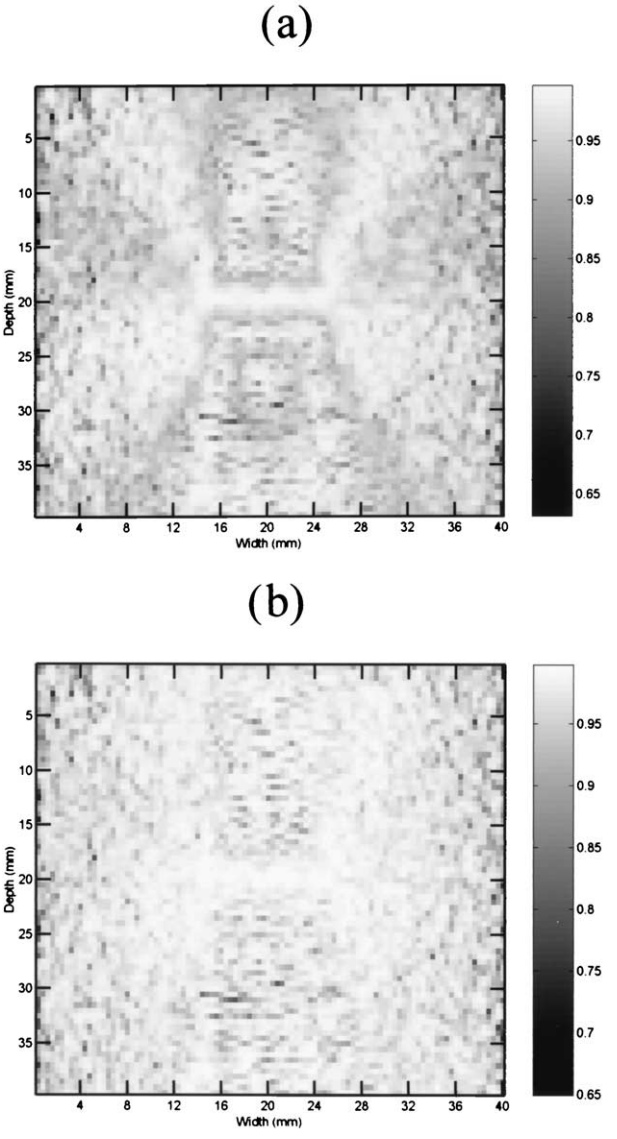

Fig. 10. Correlation maps corresponding to the elastograms simulated in Fig. 3 using (a) no interpolation, and (b) parabolic interpolation.

ing is not suitable in the presence of strain contrast.) Hence, experiments and simulations on uniformly elastic phantoms could be adequate for benchmark testing in

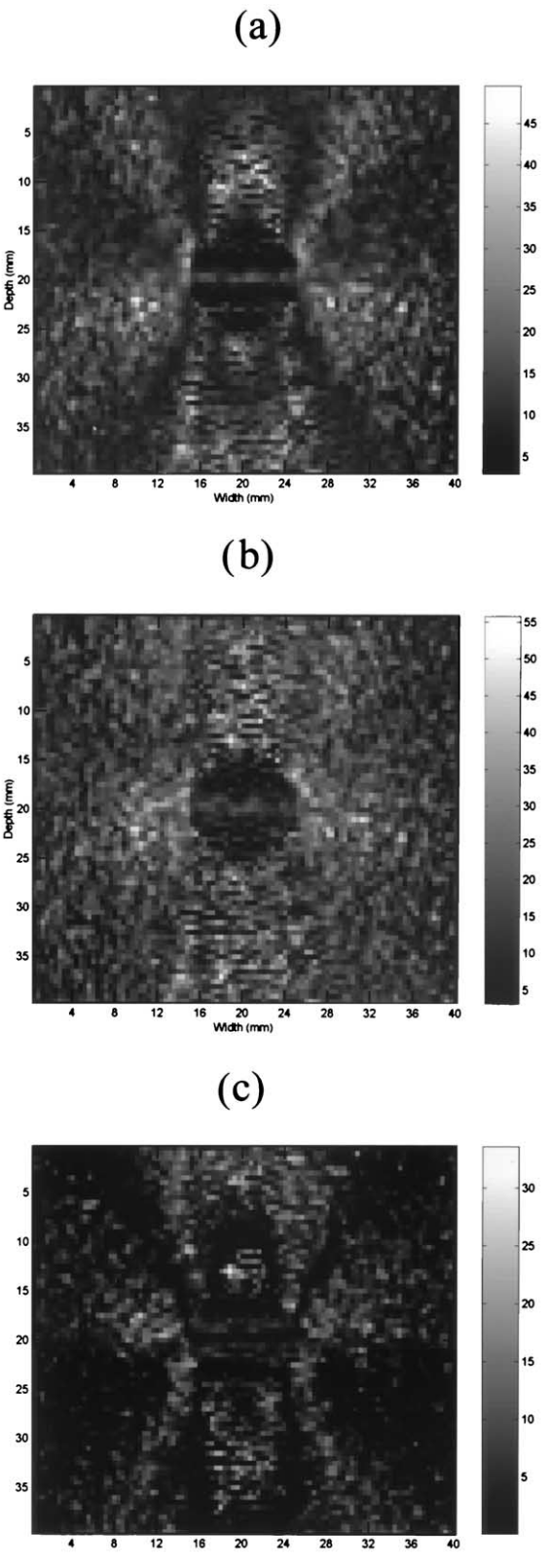

Fig. 11. SNR_e maps corresponding to the elastograms simulated in Fig. 3 using (a) no interpolation, and (b) parabolic interpolation. (c) Difference between the SNR_e maps of (b) and (a); that is, (b) − (a).

terms of the SNR_e and CNR_e. The presence of lateral and elevational motion can be included as derating factors or corrected using lateral companding (Konofagou and Ophir 1998; Chaturvedi et al. 1998) algorithms.

A major part of the study was performed using 1-D simulations instead of 2-D or 3-D simulations for two reasons: 1. Lateral and elevational motion and beam effects have been accounted for (Kallel et al. 1997) as derating factors in the SF; and 2. significantly smaller simulation time is required when statistical analysis over several parameters like the window size, overlap, center frequency, bandwidth, SNR_s, sampling frequency, quantization, *etc.* is performed.

System parameters such as f_o, B, and SNR_s are needed to use ρ to estimate SNR_e. For experimental setups, these system parameters could be found from the system specifications or measured through simple tests.

The theoretical and the simulated SFs in this work have a larger dynamic range and SNR_e values than those reported in previous works (Varghese and Ophir 1997b; Konofagou et al. 1999; Varghese et al. 2000) due to the present use of a half-power bandwidth rather than a half-amplitude bandwidth of the impulse response.

CONCLUSION

The use of the correlation coefficient to estimate the elastographic SNR (SNR_e), rather than a direct measure of SNR_e from the elastogram is shown to be robust and less sensitive to bias errors in time-delay estimation. Estimates of SNR_e computed directly from the elastograms are often higher than the theoretical upper bounds on SNR_e, due to bias errors and/or post-processing on the strain images. Using the correlation coefficient in the theoretical expressions produces strain filters that are bounded by the theoretical upper bounds. Thus ρ could be used as a benchmark in evaluating and comparing simulations and experiments to theoretical predictions. A limitation of this technique is the requirement for having access to the actual system parameters, such as the center frequency, the bandwidth, and the sonographic SNR, and not just to the final elastogram.

Acknowledgements—This work was supported by the National Cancer Institute program project P01-CA64597 awarded to the University of Texas Medical School, Houston. The authors thank R. Righetti for her helpful comments on the statistics in the paper.

REFERENCES

Alam SK, Ophir J, Konofagou E. An adaptive strain estimator for elastography. IEEE Trans Ultrason Ferroel Freq Control 1998; 45(2):461–472.

Bilgen M. Wavelet transform-based strain estimator for elastography. IEEE Trans Ultrason Ferroelec Freq Control 1999;46(6):1407–1415.

Cespedes I. Elastography. Imaging of biological tissue elasticity. Ph.D. Dissertation, University of Houston, Houston, TX, 1993.

Cespedes I, Ophir J. Reduction of image noise in elastography. Ultrason Imaging 1993;15:89–102.

Cespedes I, Huang Y, Ophir J, Spratt S. Methods for estimation of subsample time delays of digitized echo signals. Ultrason Imaging 1995a;17:142–171.

Cespedes I, Insana M, Ophir J. Theoretical bounds on strain estimation in elastography. IEEE Trans Ultrason Ferroelec Freq Control 1995b;42(5):969–972.

Chaturvedi P, Insana MF, Hall TJ. 2-D companding for noise reduction in strain imaging. IEEE Trans Ultrason Ferroelec Freq Control 1998;45(1):179–191.

de Jong PGM, Arts T, Hoeks APG, Renneman RS. Determination of tissue motion velocity by correlation interpolation of pulsed ultrasonic echo signals. Ultrason Imaging 1990;12:84–98.

Kallel F, Bertrand M, Ophir J. Fundamental limitations on the contrast-transfer efficiency in elastography: An analytic study. Ultrasound Med Biol 1996;22(4):463–470.

Kallel F, Varghese T, Ophir J, Bilgen M. The nonstationary strain filter in elastography: Part II. Lateral and elevational decorrelation. Ultrasound Med Biol 1997;23(9):1357–1369.

Konofagou EE, Ophir J. A new elastographic method for strain estimation and imaging of lateral displacements, lateral strains, corrected axial strains and Poisson's ratios in tissues. Ultrasound Med Biol 1998;24(8):1183–1199.

Konofagou EE, Varghese T, Ophir J, Alam SK. Power spectral strain estimators in elastography. Ultrasound Med Biol 1999;25(2):1115–1129.

Ophir J, Alam SK, Garra B, Kallel F, Konofagou EE, Krouskop T, Varghese T. Elastography. Ultrasonic estimation and imaging of the elastic properties of tissues. Proceedings of the Institute of Mechanical Engineering Part H. J Eng Med 1999;213:203–233.

Ophir J, Cespedes I, Garra B, Ponnekanti H, Huang Y, Maklad N. Elastography: Ultrasonic imaging of tissue strain and elastic modulus in vivo. Eur J Ultrasound 1996;3:49–70.

Ophir J, Cespedes I, Ponnekanti H, Yazdi Y, Li X. Elastography: A quantitative method for imaging the elasticity of biological tissues. Ultrason Imaging 1991;13:111–134.

Ophir J, Kallel F, Varghese T, Bertrand M, Cespedes I, Ponnekanti H. Elastography. A systems approach. Int J Imaging Syst Technol 1997;8:89–103.

Varghese T, Ophir J. Enhancement of echo-signal correlation in elastography using temporal stretching. IEEE Trans Ultrason Ferroelec Freq Control 1997a;44(1):173–180.

Varghese T, Ophir J. A theoretical framework for performance characterization of elastography: The strain filter. IEEE Trans Ultrason Ferroelec Freq Control 1997b;44(1):164–172.

Varghese T, Ophir J. An analysis of elastographic contrast-to-noise ratio. Ultrasound Med Biol 1998;24(6):915–924.

Varghese T, Konofagou EE, Ophir J, Alam SK, Bilgen M. Direct strain estimation in elastography using spectral cross-correlation. Ultrasound Med Biol 2000;26(9):1525–1537.

Weinstein E, Weiss A. Fundamental limitations in passive time delay estimation –Part I: Narrow-band systems. IEEE Trans Acoust Speech Signal Processes 1984a;31(2):472–485.

Weinstein E, Weiss A. Fundamental limitations in passive time delay estimation –Part II: Wide-band systems. IEEE Trans Acoust Speech Signal Processes 1984b;31(5):1064–1078.